WILEY | Hindawi

Research Article

Promoted Catalytic Activity of CoS$_x$@MoS$_x$/MoO$_x$ Supported on Carbon Papers for Electrocatalytic Hydrogen Evolution Reaction

Sung Hyun Hong [ID],[1] **Mahider Asmare Tekalgne** [ID],[1] **Sangwoo Ryu** [ID],[2] **Sang Hyun Ahn** [ID],[3] **and Soo Young Kim** [ID][1]

[1]*Department of Materials Science and Engineering, Korea University, 145 Anam-ro, Seongbuk-gu, Seoul 02841, Republic of Korea*
[2]*Department of Advanced Materials Engineering, Kyonggi University, Suwon 16227, Republic of Korea*
[3]*School of Chemical Engineering and Materials Science, Chung-Ang University, 84 Heukseok-ro, Dongjak-gu, Seoul 06974, Republic of Korea*

Correspondence should be addressed to Sang Hyun Ahn; shahn@cau.ac.kr and Soo Young Kim; sooyoungkim@korea.ac.kr

Developing cost-effective and stable materials for the electrocatalysis of hydrogen evolution reaction (HER) remains challenging. In this study, efficient catalysts for HER were synthesized by integrating the cobalt and molybdenum oxides via electrodeposition, followed by subsequent sulfurization of the as-prepared oxides using chemical vapor deposition (CVD). This methodology allowed the incorporation of both cobalt and molybdenum components into the catalyst in a single step. The as-synthesized CoS$_x$@MoS$_x$/MoO$_x$-based catalysts exhibited excellent hydrogen production performance in acidic media owing to the presence of Co-S and Mo-S bonds in the hybrid structure. Particularly, CoS$_x$@MoS$_x$/MoO$_x$(90@360) and MoS$_x$@CoO$_x$(180@180) displayed the best HER performances with low overpotentials of 80 mV and 150 mV, respectively. The catalysts were highly stable, with their stability preserved for over 1000 cycles with marginal reduction in overall efficiency. Therefore, these findings suggest the potential of CoS$_x$@MoS$_x$/MoO$_x$ and MoS$_x$@CoO$_x$ composites as ideal candidates for developing low-cost catalysts for electrochemical hydrogen production.

1. Introduction

The critical problems caused by climate change, the impending energy crisis, and our over-reliance on fossil fuels have triggered an investigation into the possibility of developing and utilizing alternative fuels to ensure a sustainable future [1–12]. Hydrogen is one of the alternative fuels receiving considerable attention and a huge demand owing to its clean energy and high-energy-density value [13–16]. Electrolysis can be a desirable green process for the synthesis of hydrogen, given that the energy used during the process originates from renewable energy sources such as wind or solar energy [17–20]. The hydrogen evolution reaction (HER) and the oxygen evolution reaction (OER) are the two most important reactions occurring during electrolysis. To date, noble metals, particularly platinum (Pt), with a near-zero overpotential and

a neutral hydrogen absorption energy (ΔG), act as the most efficient catalysts for HER [2, 14, 21–25]. However, the high costs of noble metals have led to a significant increase in the investigation and generation of earth-abundant catalysts to develop nonnoble metal electrocatalysts with high efficiency and the ability to function in different electrolyte solutions.

Over the past decade, nonnoble metal compounds such as transition metal dichalcogenides [26–34], carbides [35–37], transition metal phosphides [38, 39], transition metal oxides [40–44], and nitrides have proven to be effective alternatives to the noble metal-based electrocatalysts. However, the performance of nonnoble metal catalysts is still not comparable to that of noble metal-based catalysts. As a result, different techniques have been used to enhance their performance, with one technique involving the usage of heterostructures comprising multiple components with variable properties [45, 46]. These
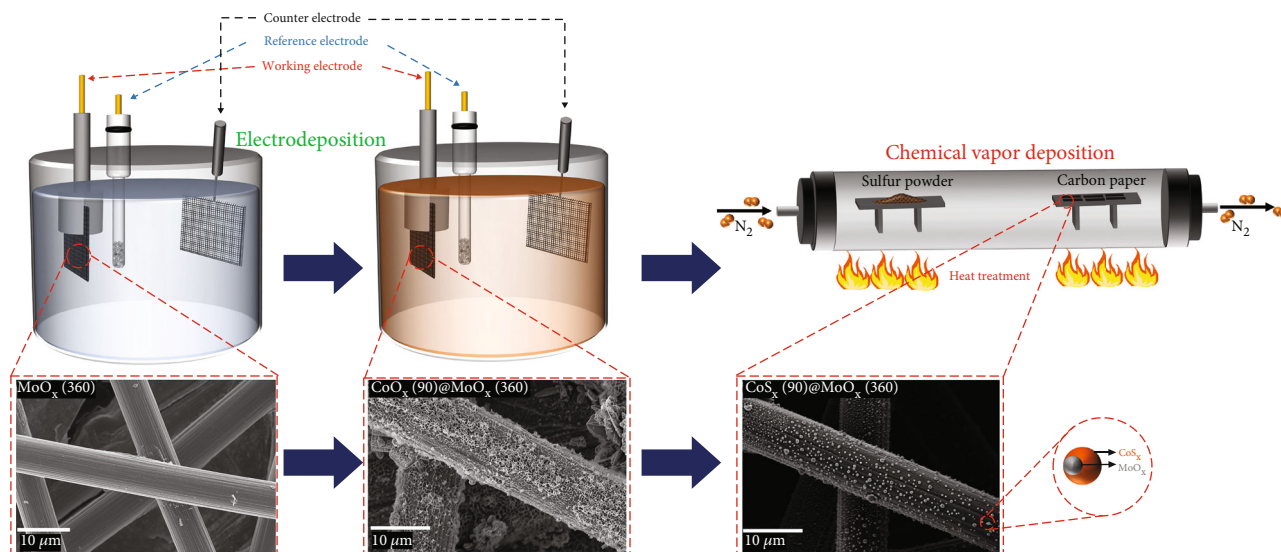
FIGURE 1: Schematic illustration of the $CoS_x@MoS_x/MoO_x$ and $MoS_x@CoO_x$ catalyst synthesis.

heterostructures possess superior electrical conductivity owing to their abundant and more exposed chemically reactive sites compared to those of their single-component counterparts [47]. Additionally, their distinctive components produce synergistic effects, boosting their electrocatalytic activity. Darshan et al. used a hydrothermal method to produce $CoS_2/MoS_2@N$-rGO-MWCNT hybrid structures [48]. The MWCNT improved the dispersion and stability, whereas rGO enhanced electrical conductivity. The presence of the N-rGO-MWCNT support increased the stability and effective loading of the CoS_2 nanoparticles, rGO, and MoS_2 nanosheets, which resulted in numerous active sites for the HER. Therefore, the results suggested that the improved electrochemical performance could be attributed to abundant active sites, synergistic effects between CoS_2 and MoS_2, and increased conductivity.

Metal oxide-based materials have garnered considerable interest owing to their utilization in a variety of applications, attributed to their advantageous compositional and structural diversity, flexible tunability, low cost, earth-abundance, ease of synthesis, and environmental friendliness [21, 49, 50]. However, bare and pure metal oxides, particularly bulk materials, are inactive toward the HER because of their poor electrical conductivity and limited number of catalytically active sites, although several of them display high activity for the anodic OER. Therefore, their catalytic performance is enhanced using methods such as doping, hybridization, and surface reconstruction of metal oxides [40].

In this study, we proposed a simple method for producing $CoS_x@MoS_x/MoO_x$ and $MoS_x@CoO_x$ (Figure 1) electrocatalysts, with $CoO_x@MoO_x$ and $MoO_x@CoO_x$ prepared via electrodeposition at room temperature followed by their sulfurization, yielding $CoS_x@MoS_x/MoO_x$ and $MoS_x@CoO_x$, respectively, as products. Chemical vapor deposition was used to grow CoS_x and MoS_x nanosheets on the surfaces of cobalt and molybdenum oxides. The unique $CoS_x@MoS_x/MoO_x$ and $MoS_x@CoO_x$ heterostructures acted as efficient electrocatalysts for the HER.

2. Experimental Section

2.1. Material Synthesis

2.1.1. Electrode Preparation. The substrate (carbon cloth) was cut into $1 \times 1 \, cm^2$ pieces, washed sequentially in deionized water and acetone for 5 min using sonication, and blow-dried with N_2 before use.

2.1.2. Electrodeposition of Heterostructure Catalyst on the Electrode. The electrodeposition process involved two steps for the fabrication of $CoO_x@MoO_x$ and $MoO_x@CoO_x$ heterostructures on carbon paper (CP) substrates. A mixture of H_2SO_4 (95–98%) and 30% HNO_3 (70%) was used in a $3:1$ ratio to enhance the hydrophilicity of the substrate, and the CP was immersed in this solution for 30 min at 60°C. Electrodeposition was performed using a three-electrode cell system composed of the pretreated CP with an exposed area of $6 \, cm^2$ as the working electrode, a Pt mesh as the counter electrode, and a saturated calomel electrode (SCE) as the reference electrode. 100 mM $CoSO_4 \cdot 7H_2O$ and 100 mM $Na_2MoO_4 \cdot 4H_2O$ dissolved in deionized (DI) water were used as deposition electrolytes. Before deposition, the electrolyte was purged using N_2 gas for 30 min to eliminate the dissolved oxygen. Deposition was performed by varying the deposition time (90, 180, 360, and 540 s) at -2.0 V_{SCE} in the $Na_2MoO_4 \cdot 4H_2O$ electrolyte followed by drying on a hot plate at 60°C for 1 h. Subsequent electrodeposition was performed in the $CoSO_4 \cdot 7H_2O$ electrolyte under the same conditions as described above to oxidize Co into CoO_x, generating $CoO_x@MoO_x$ (Figure 1). The electrodeposition order was reversed to fabricate $MoO_x@CoO_x$ structures following the same procedure, resulting in 16 different electrodes based on the plating time. The electrodes were denoted as $CoO_x(90–360)@MoO_x(90–360)$ and $MoO_x(90–360)@CoO_x(90–360)$. Subsequently, the as-synthesized $CoO_x(90–360)@MoO_x(90–360)$ and $MoO_x(90–360)@CoO_x(90–360)$ along with sulfur powders

($\geq$99.0%) were placed upstream and downstream of a tune furnace and heated to 800°C for 2 h under N_2 environment to afford the $CoS_x@MoO_x$ and $MoS_x@CoO_x$ heterostructures, respectively.

2.2. Characterization. Cu K radiation (=0.154 nm) was used for the X-ray diffraction (XRD; Bruker New D8-Advance, Seoul, Korea) analysis of the crystal structure of the as-prepared catalyst. A Raman analyzer (LabRAM-HR Evolution) was used to get Raman spectra. To examine the morphology of the prepared samples, field emission scanning electron microscopy (FESEM; Zeiss 300 VP, Seoul, Korea) images were collected. The X-ray photoelectron spectroscopy (XPS) method was used to confirm the elemental composition and oxidation states of the catalysts. The morphology was also confirmed by transmission electron microscopy (TEM).

2.3. Electrochemical Measurement. Using a potentiostat workstation (Ivium 5612), the HER performance of the catalysts was evaluated in an acidic (0.5 M H_2SO_4) electrolyte solution. The counter, reference, and working electrodes were carbon rods, a saturated calomel electrode (SCE), and the as-prepared electrode (with a working area of $0.5 \times 0.5 \, cm^2$). The data for the electrochemical impedance spectroscopy (EIS) graphs were collected within a frequency range of 0.1–100 kHz. Cyclic voltammetry (CV) in the potential window of 0.1–0.3 V vs. reversible hydrogen electrode (RHE) at a scan rate of 100 mV/s and chronoamperometry for 12 h at a constant voltage were performed to evaluate the long-term quality and stability of the working electrode.

RHE (reversible hydrogen electrode) potentials were calculated using the following formula: potential (E) vs. RHE (V) = E vs. SCE (saturated calomel electrode) + E°(SCE) + 0.059 pH (V). All the electrochemical data are reported without iR compensation.

3. Results and Discussion

The fabrication of $CoS_x@MoS_x/MoO_x$ and $MoS_x@CoO_x$ heterostructures is schematically illustrated in Figure 1. Before sulfurization, CoOx and MoOx are electrochemically deposited. Field emission scanning electron microscopy (FESEM) was conducted to confirm the formation of the hybrid structure. The thickness of the nanoparticle layer increases with an increase in electrodeposition time for Co, forming a thick film after sulfurization (Figure S1). In contrast, Mo deposition on CP remains flat even with an increase in plating time; however, after thermal treatment, the Mo particles agglomerate, ranging in size from several to tens of nanometers (Figure S2). The shape and structure of the catalyst vary depending upon the Co plating time, even after sulfurization (Figure S3, S4). Additionally, the structure depends on the Co and Mo deposition sequences. When Mo is deposited for 360 s, followed by Co deposition for 90 s, the resulting structure closely resembles that of Co deposition for 90 s. However, the $CoS_x(90)$ particles agglomerate significantly after heat treatment, whereas the

particle size of $CoS_x(90)@MoO_x(360)$ reduces to tens of nanometers (Figure 2(b) and Figure S1). When Co is electrodeposited for 180 s, followed by Mo deposition for 180 s, the structure differs from that of Co deposition alone and remains distinct after heat treatment (Figures 2(d)–2(f) and Figure S2). The increase in deposition time of Co to 360 s results in the formation of a thick film over the entire substrate, regardless of the plating order (Figure S5, S6).

The XRD patterns of $CoS_x@MoO_x(90-90)$, $CoS_x@MoO_x(90-180)$, and $CoS_x@MoO_x(90-360)$ are shown in Figure 3(a). The peaks at 2θ values of 11.1° and 26.1° can be indexed to the (020) and (040) planes, respectively, of molybdenum oxide [51]. The XRD pattern of $CoS_x@MoO_x$ exhibits a peak at 53.9° corresponding to the (221) plane of CoS_x [52]. The XRD patterns of $CoS_x@MoO_x$ (90-360) showed a similar structure after stability maintaining its original structure (Figure S6). The TEM image of $CoS_x@MoS_x/MoO_x$ (Figures 3(b)–3(d)) and the elemental mapping images of Co, Mo, S, C, and O (Figure 3(e)) further confirm that the product is successfully obtained and comprises the exact elements in the selected area of the sample ($CoS_x@MoS_x/MoO_x(90@360)$).

CoS_x, MoS_x, $CoS_x@MoS_x/MoO_x$, and $MoS_x@CoO_x$ were further investigated using XPS to determine the elemental states and chemical compositions. Figure S7 confirms the successful growth of CoS_x as demonstrated by the existence of peaks corresponding to Co $2p_{1/2}$ and $2p_{3/2}$. The presence of peaks assigned to S $2p_{1/2}$, S $2p_{3/2}$, and S-O further confirms the formation of CoS_x. However, Figure S8 reveals that MoO_x is not fully converted to MoS_x because the intensity of the S 2p peak is almost negligible; therefore, it shows the lowest performance among the synthesized samples. Figure S9 displays the XPS spectra of Mo 3d and Co 2p, and O 1s in the as-synthesized MoO_x/CoO_x. The peaks at 234.9 and 231.7 eV correspond to Mo^{4+} $3d_{3/2}$ and Mo^{4+} $3d_{5/2}$, respectively, whereas the peaks at 796.8 and 780.9 eV could be assigned to Co $2p_{1/2}$ and $2p_{3/2}$, respectively. After sulfurization, the S 2p high-resolution XPS spectrum displays two peaks at 169.8 and 163.1 eV corresponding to S-O and S $2p_{1/2}$, respectively, and a satellite peak at 161.2 eV (Figure S10). The XPS survey spectrum in Figure 4(a) reveals the trace of Co, Mo, S, C, and O elements in $CoS_x@MoS_x/MoO_x$. Long-term exposure to air results in the presence of carbon and oxygen elements. The Co^{2+} is characterized by peaks at 781.4 eV (Co $2p_{3/2}$) and 796.9 eV (Co $2p_{1/2}$) (Figure 4(b)) [53], which shift to a higher energy state after the sulfurization of CoO_x/MoO_x as compared to the two peaks at 781.0 and 796.7 eV corresponding to Co $2p_{3/2}$ and Co $2p_{1/2}$ in CoO_x/MoO_x before sulfurization, respectively (Figure S11). The Co^{3+} is characterized by two peaks at 779.1 eV (Co $2p_{3/2}$) and 794.1 eV (Co $2p_{1/2}$) along with satellite peaks at 785.8 and 803.6 eV. The Mo 3d XPS spectrum exhibits peaks at 232.7 and 229.5 eV ascribed to Mo $3d_{3/2}$ and Mo $3d_{5/2}$, respectively, corresponding to Mo^{4+}. Additionally, the peaks at 226.5 and 235.7 eV could be attributed to the Mo-S bond and the Mo^{6+} state, respectively, with Mo^{6+} originating from MoO_x indicating the formation of oxygen bonds in the hybrid structure (Figure 4(c)) [54]. The HER activities were
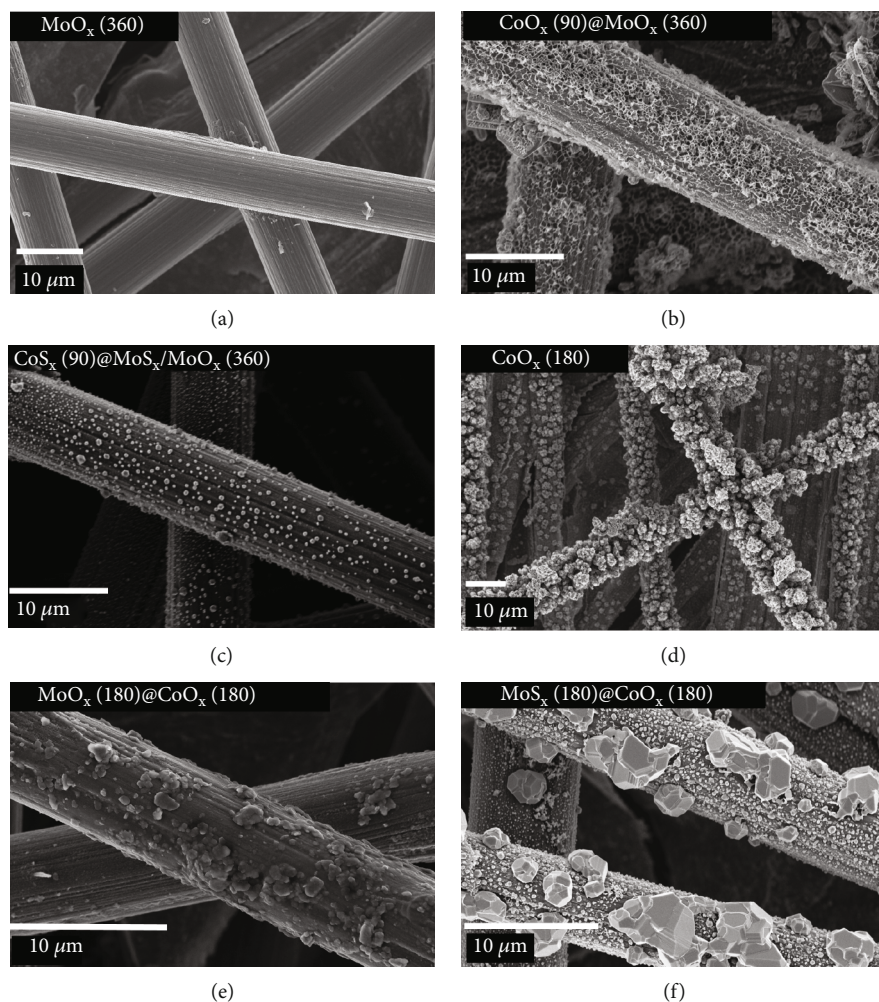
Figure 2: FESEM images of (a) $MoO_x(360)$, (b) $CoO_x(90)@MoO_x(360)$, (c) $CoO_x(90)@MoS_x/MoO_x(360)$, (d) $CoO_x(180)$, (e) $MoO_x(180)@CoO_x(180)$, and (f) $MoS_x(180)@MoO_x(180)$.

enhanced by the existence of Mo-S and Mo-O bonds in the hybrid structure, in addition to the Co-S bond. The XPS spectrum of S 2p corresponding to the Mo-S bonds in MoS_x/MoO_x shows a peak at the binding energy of 162.3 eV ascribed to S $2p_{3/2}$, whereas a smaller peak positioned at 163.7 eV is assigned to S $2p_{1/2}$. Similarly, the peaks belonging to S $2p_{3/2}$ and S $2p_{1/2}$ of the Co-S bonds in CoS_x are found at 161.8 and 163.5 eV, respectively (Figure 4(d)). Figure 4(e) displays the XPS spectrum of O 1s showing the presence of oxygen at the surface of the as-prepared catalyst.

A series of tests were performed to evaluate the electrochemical performance of $MoS_x@CoO_x(90, 180, 360@90, 180, 360)$ and $CoS_x@MoS_x/MoO_x(90, 180, 360@90, 180, 360)$ nanocomposites for the HER. Pristine CoS_x (90, 180) and MoS_x (180, 360) were prepared using the same method for comparison. The HER activity of the as-synthesized catalysts was investigated in a 0.5 M H_2SO_4 solution using a three-electrode setup, where the as-synthesized sample-coated carbon cloth electrode was used as the working electrode. Figure 5(a) displays the polarization curves of $CoS_x(90)$, $CoS_x(180)$, $MoS_x(180)$, $MoS_x(360)$, $MoS_x@CoO_x(180@180)$,

and $CoS_x@MoS_x/MoO_x(90@360)$. $MoS_x(180)$ shows low catalytic activity for hydrogen evolution, whereas the $CoS_x@MoS_x/MoO_x(90@360)$ electrode exhibits the best HER yield. MoS_x (180) shows poor HER catalytic performance as compared to that of CoS_x as it contains more oxide components, resulting in fewer catalytically active sites. Figure S12 shows that the overpotentials at 10 and 20 mA/cm^2 for $CoS_x@MoS_x/MoO_x(90@360)$ are 80 and 250 mV, respectively, whereas those for $MoS_x@CoO_x(180@180)$ are 150 and 260 mV, respectively. The potential for the $MoS_x@CoO_x$ and $CoS_x@MoO_x$ hybrid structure of different deposition time at 10 and 20 mA/cm^2 is listed in Table S1 and Table S2. Pristine CoS_x and MoS_x at different depositions show much higher potentials than that of the hybrid structure. The electrocatalytic performances of the other hybrid structures of MoS_x and CoS_x at different depositions are shown in Figure S13 and S14. A comparison of the overpotentials with other known electrocatalysts is given in Figure 5(b) [55–58].

EIS was used to investigate the electrode kinetics during the HER process at -0.2 V vs. RHE to better understand the
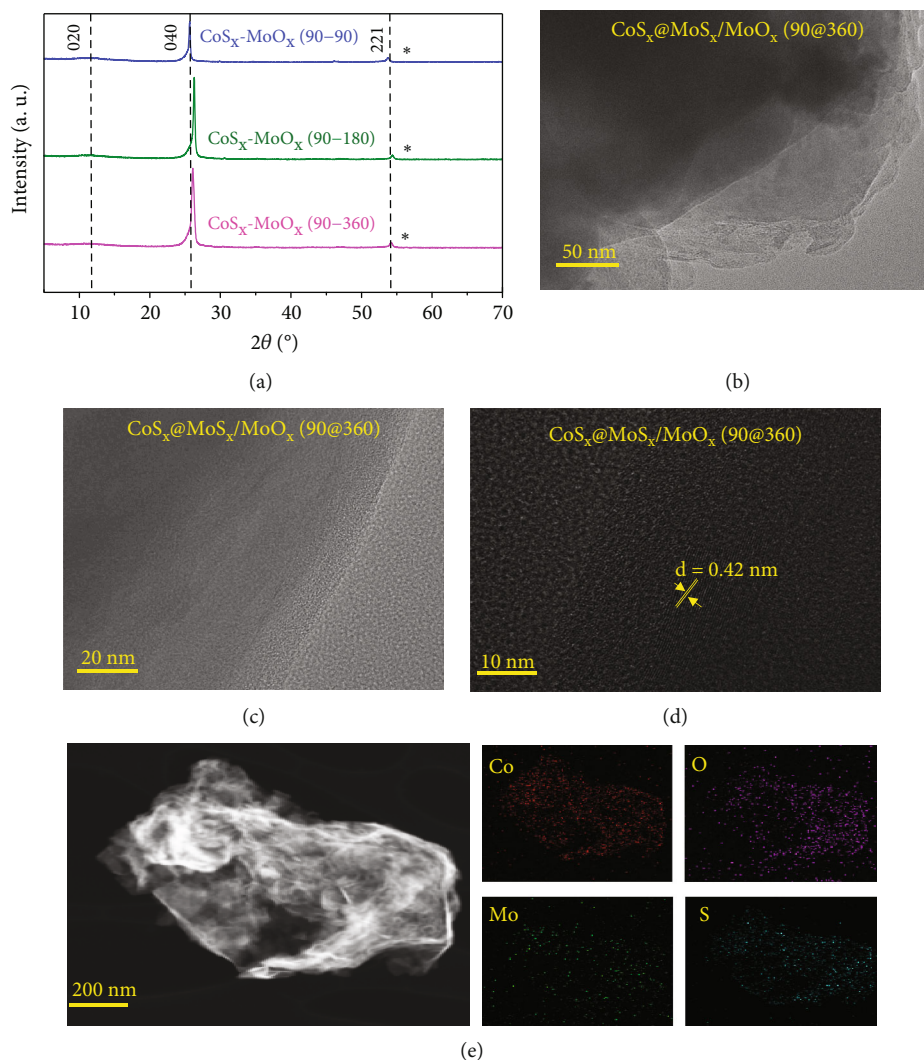
(a)

(b)

(c)

(d)

(e)

Figure 3: (a) XRD patterns of CoSx@MoOx (90@90), (90@180), and (90@360); (b, c) TEM; (d) HRTEM; and (e) EDS elemental mapping images of $CoS_x@MoS_x/MoO_x(90@360)$.

electrocatalytic process. The semicircles reflect the charge transfer resistance (R_{ct}) across the electrocatalyst/electrolyte interface, and the catalytic activities can be determined from these resistances. Figure 5(c) shows the EIS spectra of the samples, which are fitted with an equivalent circle (inset of Figure 5(c)) to determine the Rct. The R_{ct} value for $CoS_x@MoS_x/MoO_x(90@360)$ is $25\,\Omega$, which is much lower than that of $MoS_x@CoO_x$ (180@180) ($60\,\Omega$) and $MoS_x@CoO_x(90@90)$ ($300\,\Omega$). During the electrocatalytic process, the $CoS_x@MoS_x/MoO_x(90@360)$ catalyst exhibits the fastest interfacial charge transport kinetics because it has the lowest R_{ct}. However, the R_{ct} value of $CoS_x@MoS_x/MoO_x$ (90@360) increased after the HER measurement as shown in Figure S15. The R_{ct} values for other samples are shown in Figure S16 and S17. The R_{ct} values compared to catalysts are shown in Table S3.

The electrochemically active surface area (ECSA) is responsible for the observed variations in the HER catalytic efficacy of the working electrodes [59, 60]. A cyclic volt-

ammetry (CV) analysis was conducted to determine the ECSA, which is closely related to the double-layer capacitance (C_{dl}). CV measurements were conducted within a specific potential range of $0.1–0.2\,V$ vs. RHE at seven distinct scan rates ($20–150\,mV/s$), focusing entirely on nonfaradaic current. C_{dl} is represented by the slope of the plot in Figure 5(d), which depicts the variation in the current density with respect to the scan rate. Notably, the C_{dl} value of $CoS_x@MoS_x/MoO_x(90@360)$ is $6.3\,mF/cm^2$, which is approximately four times greater than that of $MoS_x@CoO_x(180@180)$ ($1.6\,mF/cm^2$). This significant observation demonstrates that $CoS_x@MoS_x/MoO_x(90@360)$ has the greatest effective surface area, confirming a strong relationship between ECSA and catalytic properties. The turnover frequencies (TOFs) were calculated using a formula established in a previous study [31]. The values are $0.01\,s^{-1}$ and $0.04\,s^{-1}$ for $CoS_x@MoO_x(90@360)$ and $MoS_x@CoO_x(180@180)$, respectively. It is plotted in a bar diagram of Figure 5(e), with $CoS_x@MoO_x(90@360)$ showing higher activity.
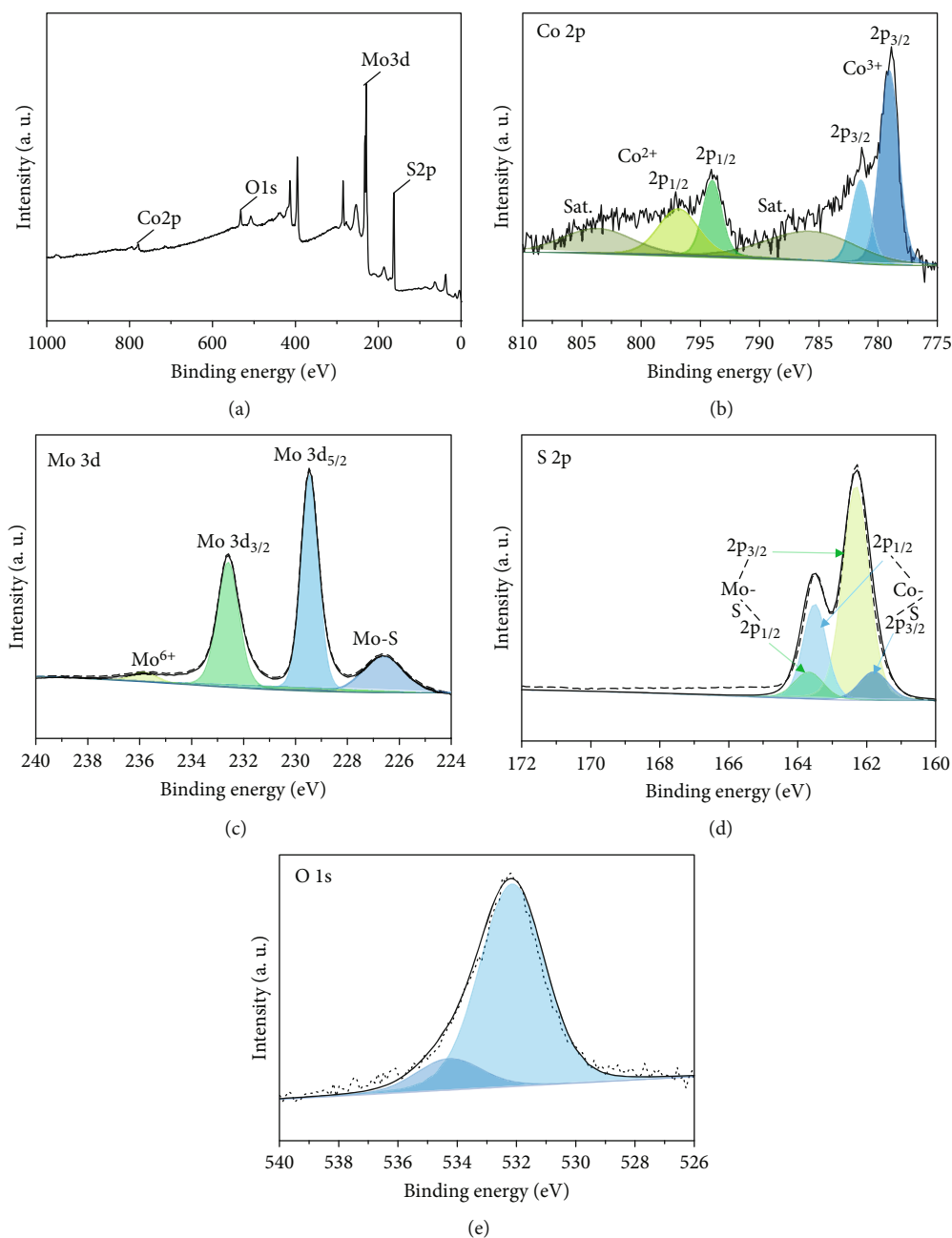
Figure 4: XPS spectra of (a) survey, (b) Co 2p, (c) Mo 3d, (d) S 2p, and (e) O 1s in $CoS_x@MoS_x/MoO_x(90@360)$.

High stability is a crucial catalyst property for enabling utilization in practical applications. A durability test was conducted for the $CoS_x@MoS_x/MoO_x(90@360)$ catalyst subjected to continuous CV cycles at a scan rate of 50 mV/s in a 0.5 M H_2SO_4 solution. This test determines the extent to which the catalyst remains effective. The polarization curve after 1000 CV cycles closely resembled the initial curve obtained before CV measurement, as shown in Figure 5(f). This indicates a negligible decrease in current density and confirms the outstanding stability of $CoS_x@MoS_x/MoO_x(90@360)$ under acidic conditions. Additionally, the current-time responses demonstrated that

the electrocatalytic activity of $CoS_x@MoS_x/MoO_x(90@360)$ could be preserved for at least 24 h in an acidic solution.

4. Conclusions

In this study, the $CoS_x@MoS_x/MoO_x$ and $MoS_x@CoO_x$ hybrid structures were successfully fabricated from $CoO_x@MoO_x$ and $MoO_x@CoO_x$, respectively, and used as effective electrocatalysts for HER in acidic environments. The studies revealed a considerably higher HER activity of $CoS_x@MoS_x/MoO_x$ compared to those of $MoS_x@CoO_x$, $CoO_x@MoO_x$, and $MoO_x@CoO_x$ catalysts. Notably, $CoS_x@MoS_x/MoO_x$

(a)

(b)

(c)

(d)

(e)

(f)
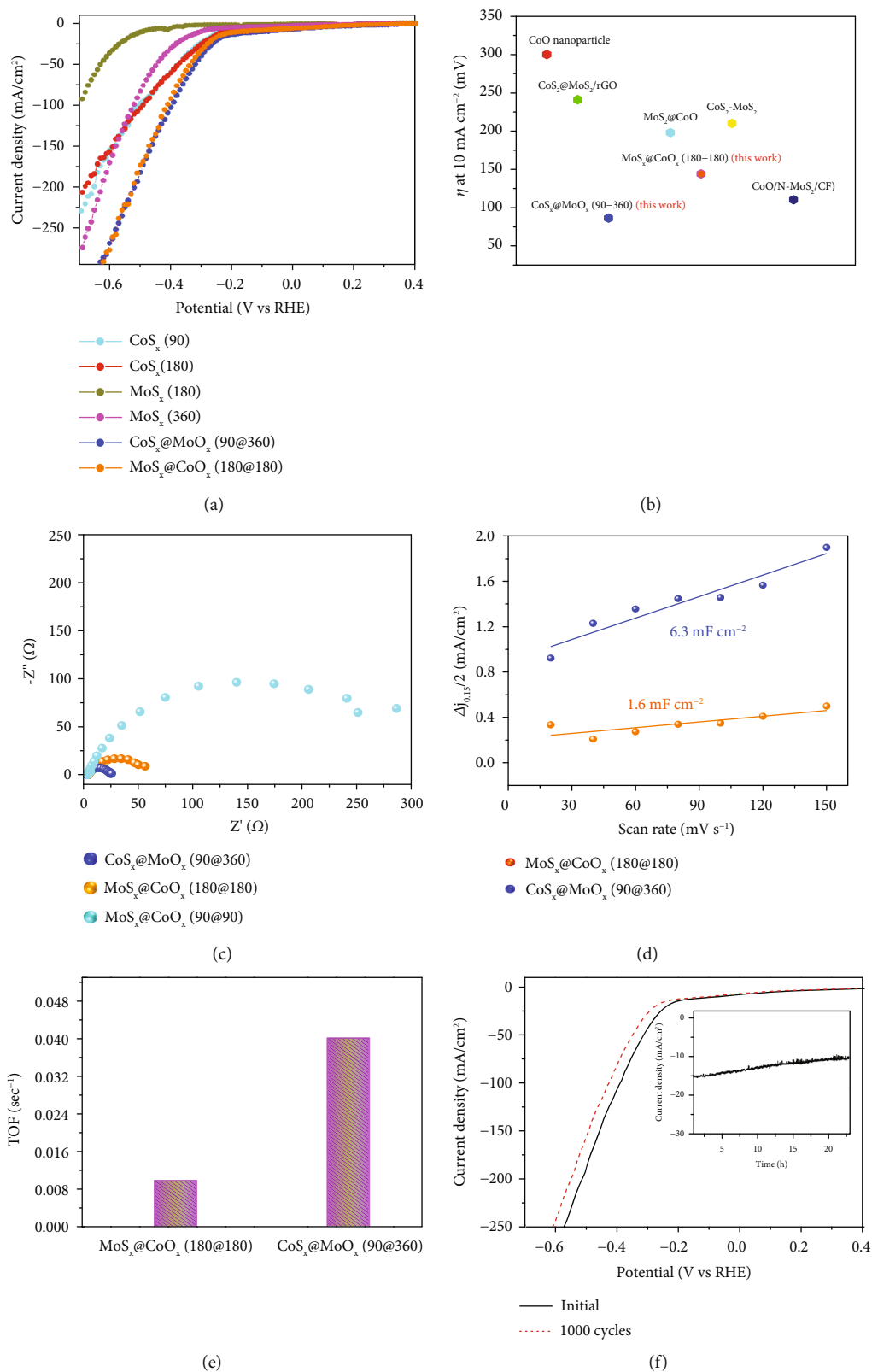
FIGURE 5: (a) LSV curves and (b) comparison of the overpotential required to achieve a current density of 10 mA/cm^2 with reported papers; (c) EIS spectra of MoS$_x$@CoO$_x$(90-90), MoS$_x$@CoO$_x$(180-180), and CoS$_x$@MoO$_x$(90-360) at −0.3 V vs. RHE in 0.5 M H$_2$SO$_4$; (d) double-layer capacitance (C_{dl}) of MoSx@CoOx(180-180) and CoSx@MoOx(90-360) at 0.15 V vs. RHE as a function of the scan rate 50 mV/s; (e) TOF plot of MoS$_x$@n(180-180) and CoS$_x$@MoO$_x$(90-360); (f) polarization curves of CoS$_x$@MoO$_x$(90-360) catalysts before and after 1000 CV cycles (inset: chronoamperometry test for 24 h).

(90@360) displayed a very low overvoltage of 80 mV at a current density of 10 mA/cm^2. Following a test period of 24 h, the catalyst exhibited outstanding stability. The excellent HER activity could be attributed to the sulfurized CoS_x and MoS_x, both of which aided the formation of Co-S and Mo-S bonds in the hybrid structure, resulting in a large surface area. Thus, these results highlight the potential of $CoS_x@MoS_x/MoO_x$ and $MoS_x@CoO_x$ composites as ideal candidates for developing low-cost catalysts for electrochemical hydrogen production.

Data Availability

The data used to support the findings of this study are included within the manuscript and the supplementary information files.

Disclosure

This manuscript was submitted as a preprint in the link "https://www.researchgate.net/publication/373341121_Promo ted_Catalytic_Activity_of_CosxMosxMoox_Supported_on_ Carbon_Papers_for_Electrocatalytic_Hydrogen_Evolution_ Reaction."

Conflicts of Interest

The authors declare that they have no conflicts of interest.

Authors' Contributions

Sung Hyun Hong and Mahider Asmare Tekalgne were responsible for conceptualization, data curation, formal analysis, investigation, methodology, visualization, and writing the original draft. Sangwoo Ryu was responsible for formal analysis and writing. Sang Hyun Ahn was responsible for writing, reviewing, editing, supervision, and project administration. Soo Young Kim was responsible for writing, reviewing, editing, supervision, and project administration. Sung Hyun Hong and Mahider Asmare Tekalgne contributed equally to this work.

Acknowledgments

Supplementary Materials

Figure S1: FESEM images of CoO_x. Figure S2: FESEM images of MoO_x. Figure S3: FESEM images of $MoO_x@CoO_x$ and $MoO_x@CoO_x$. Figure S4: FESEM images of $CoS_x@MoO_x$. Figure S5: FESEM images of $MoS_x@CoO_x$. Figure S6: XRD patterns of $CoS_x@MoO_x$. Figure S7: XPS spectra of CoS_x. Figure S8: XPS spectra of MoS_x. Figure S9: XPS spectra of $MoO_x@CoS_x$. Figure S10: XPS spectra of $MoS_x@CoO_x$. Figure S11: XPS spectra of $CoO_x@MoS_x$. Figure S12: overpotential at 10 and 20 mA/cm^2. Figure S13: LSV curves of $MoS_x@CoO_x$. Figure S14: EIS spectra of $MoS_x@CoO_x$.

Figure S15: EIS spectra of $CoS_x@MoO_x$. Figure S16: LSV curves of $CoS_x@MoO_x$. Figure S17: EIS spectra of $CoS_x@MoO_x$. Table S1: electrocatalytic HER performance of the prepared $MoS_x@CoO_x$. Table S2: electrocatalytic HER performance of the prepared $CoS_x@MoO_x$. Table S3: comparison of charge transfer resistances (Rct). (Supplementary Materials)

References

[1] K. Karuppasamy, V. R. Jothi, D. Vikraman et al., "Metal-organic framework derived NiMo polyhedron as an efficient hydrogen evolution reaction electrocatalyst," Applied Surface Science, vol. 478, pp. 916–923, 2019.

[2] J. Zhu, L. Hu, P. Zhao, L. Y. S. Lee, and K.-Y. Wong, "Recent advances in electrocatalytic hydrogen evolution using nanoparticles," Chemical Reviews, vol. 120, no. 2, pp. 851–918, 2020.

[3] A. B. Laursen, S. Kegnæs, S. Dahl, and I. Chorkendorff, "Molybdenum sulfides—efficient and viable materials for electro - and photoelectrocatalytic hydrogen evolution," Energy & Environmental Science, vol. 5, no. 2, pp. 5577–5591, 2012.

[4] X. Chen, L. Liu, P. Y. Yu, and S. S. Mao, "Increasing solar absorption for photocatalysis with black hydrogenated titanium dioxide nanocrystals," Science, vol. 331, no. 6018, pp. 746–750, 2011.

[5] J. Liu, Y. Liu, N. Liu et al., "Metal-free efficient photocatalyst for stable visible water splitting via a two-electron pathway," Science, vol. 347, no. 6225, pp. 970–974, 2015.

[6] M. S. Faber and S. Jin, "Earth-abundant inorganic electrocatalysts and their nanostructures for energy conversion applications," Energy Environment Science, vol. 7, no. 11, pp. 3519–3542, 2014.

[7] Y. Jiao, Y. Zheng, M. Jaroniec, and S. Z. Qiao, "Design of electrocatalysts for oxygen- and hydrogen-involving energy conversion reactions," Chemical Society Reviews, vol. 44, no. 8, pp. 2060–2086, 2015.

[8] V.-H. Nguyen, B.-S. Nguyen, Z. Jin et al., "Towards artificial photosynthesis: sustainable hydrogen utilization for photocatalytic reduction of CO_2 to high-value renewable fuels," Chemical Engineering Journal, vol. 402, article 126184, 2020.

[9] T. P. Nguyen, D. L. T. Nguyen, V.-H. Nguyen et al., "Recent advances in TiO_2-based photocatalysts for reduction of CO_2 to fuels," Nanomaterials, vol. 10, no. 2, p. 337, 2020.

[10] H. H. Do, D. L. T. Nguyen, X. C. Nguyen et al., "Recent progress in TiO2-based photocatalysts for hydrogen evolution reaction: a review," Arabian Journal of Chemistry, vol. 13, no. 2, pp. 3653–3671, 2020.

[11] V.-H. Nguyen, B.-S. Nguyen, C.-C. Hu et al., "Novel architecture titanium carbide ($Ti_3C_2T_x$) MXene cocatalysts toward photocatalytic hydrogen production: a mini-review," Nanomaterials, vol. 10, no. 4, p. 602, 2020.

[12] S. Bae, S. Lee, H. Ryu, and W.-J. Lee, "Improvement of photoelectrochemical properties of CuO photoelectrode by Li doping," Korean Institute of Metals and Materials, vol. 60, no. 8, pp. 577–586, 2022.

[13] Y. Kumaran, T. Maiyalagan, and S. C. Yi, "An efficientCo-MoS2nanosheets on nitrogen, sulfur dual doped reduced graphene oxide as an electrocatalyst for the hydrogen evolution reaction," International Journal of Energy Research, vol. 45, no. 12, pp. 17397–17407, 2021.

[14] X. Zou and Y. Zhang, "Noble metal-free hydrogen evolution catalysts for water splitting," *Chemical Society Reviews*, vol. 44, no. 15, pp. 5148–5180, 2015.

[15] B. Zhang, C. Li, G. Yang et al., "Nanostructured CuO/C hollow shell@3D copper dendrites as a highly efficient electrocatalyst for oxygen evolution reaction," *ACS Applied Material Interfaces*, vol. 10, no. 28, pp. 23807–23812, 2018.

[16] S. A. Shah, L. Xu, R. Sayyar et al., "Growth of MoS2 nanosheets on M@ N-doped carbon particles (M= Co, Fe or CoFe alloy) as an efficient electrocatalyst toward hydrogen evolution reaction," *Journal of Chemical Engineering*, vol. 428, article 132126, 2022.

[17] J. Wang, W. Cui, Q. Liu, Z. Xing, A. M. Asiri, and X. Sun, "Recent progress in cobalt-based heterogeneous catalysts for electrochemical water splitting," *Advanced Materials*, vol. 28, no. 2, pp. 215–230, 2016.

[18] P. C. Vesborg, B. Seger, and I. Chorkendorff, "Recent development in hydrogen evolution reaction catalysts and their practical implementation," *Journal of Physical Chemistry Letters*, vol. 6, no. 6, pp. 951–957, 2015.

[19] Y. Cheng, S. Lu, F. Liao, L. Liu, Y. Li, and M. Shao, "Rh–MoS2 nanocomposite catalysts with Pt-like activity for hydrogen evolution reaction," *Advanced Functional Materials*, vol. 27, no. 23, p. 1700359, 2017.

[20] Q. Liu, J. Shi, J. Hu, A. M. Asiri, Y. Luo, and X. Sun, "CoSe2 nanowires array as a 3D electrode for highly efficient electrochemical hydrogen evolution," *ACS Applied Material Interfaces*, vol. 7, no. 7, pp. 3877–3881, 2015.

[21] R. Subbaraman, D. Tripkovic, D. Strmcnik et al., "Enhancing hydrogen evolution activity in water splitting by tailoring Li +-Ni(OH)2-Pt interfaces," *Science*, vol. 334, no. 6060, pp. 1256–1260, 2011.

[22] X. Han, X. Wu, Y. Deng et al., "Ultrafine Pt nanoparticle-decorated pyrite-type CoS2 nanosheet arrays coated on carbon cloth as a bifunctional electrode for overall water splitting," *Advanced Functional Materials*, vol. 8, article 1800935, 2018.

[23] P. Zhou, F. Lv, N. Li et al., "Strengthening reactive metal-support interaction to stabilize high-density Pt single atoms on electron-deficient g-C3N4 for boosting photocatalytic H2 production," *Nano Energy*, vol. 56, pp. 127–137, 2019.

[24] J. Xie, H. Zhang, S. Li et al., "Defect-rich MoS2 ultrathin nanosheets with additional active edge sites for enhanced electrocatalytic hydrogen evolution," *Advanced Materials*, vol. 25, no. 40, pp. 5807–5813, 2013.

[25] Z. Li, J.-Y. Fu, Y. Feng, C.-K. Dong, H. Liu, and X. W. du, "A silver catalyst activated by stacking faults for the hydrogen evolution reaction," *Nature Catalysis*, vol. 2, no. 12, pp. 1107–1114, 2019.

[26] K. Zhang, B. Jin, Y. Gao et al., "Aligned heterointerface-induced 1T-MoS2Monolayer with near-ideal Gibbs free for stable hydrogen evolution reaction," *Small*, vol. 15, no. 8, article 1804903, 2019.

[27] I.-W. P. Chen, C.-H. Hsiao, J.-Y. Huang, Y.-H. Peng, and C. Y. Chang, "Highly efficient hydrogen evolution from seawater by biofunctionalized exfoliated MoS2 quantum dot aerogel electrocatalysts that is superior to Pt," *ACS Applied Material Interfaces*, vol. 11, no. 15, pp. 14159–14165, 2019.

[28] G. Wang, W. Chen, G. Chen et al., "Trimetallic Mo–Ni–Co selenides nanorod electrocatalysts for highly-efficient and ultrastable hydrogen evolution," *Nano Energy*, vol. 71, no. 2020, article 104637, 2020.

[29] X. Feng, Q. Jiao, T. Liu et al., "Facile synthesis of Co9S8 hollow spheres as a high-performance electrocatalyst for the oxygen evolution reaction," *ACS Sustainable Chemical Engineering*, vol. 6, no. 2, pp. 1863–1871, 2018.

[30] A. Hasani, Q. V. Le, M. Tekalgne et al., "Direct synthesis of two-dimensional MoS2 on p-type Si and application to solar hydrogen production," *NPG Asia Materials*, vol. 11, no. 1, p. 47, 2019.

[31] T. Van Nguyen, H. H. Do, M. Tekalgne et al., "WS2-WC-WO3 nano-hollow spheres as an efficient and durable catalyst for hydrogen evolution reaction," *Nano Convergence*, vol. 8, no. 1, pp. 1–12, 2021.

[32] C. Liu, C. Kong, F.-J. Zhang et al., "Research progress of defective MoS2 for photocatalytic hydrogen evolution," *Journal Korean Ceramics Society*, vol. 58, no. 2, pp. 135–147, 2021.

[33] T. Van Nguyen, T. P. Nguyen, Q. Van Le, D. Van Dao, S. H. Ahn, and S. Y. Kim, "Synthesis of very small molybdenum disulfide nanoflowers for hydrogen evolution reaction," *Applied Surface Science*, vol. 607, article 154979, 2023.

[34] H. H. Do, T. D. C. Ha, H. Jo et al., "Low-temperature synthesis of molybdenum sulfides, tungsten sulfides, and composites thereof as efficient electrocatalysts for hydrogen evolution reaction," *Applied Surface Science*, vol. 576, article 151828, 2022.

[35] Y. Yu, J. Zhou, and Z. Sun, "Novel 2D transition-metal carbides: ultrahigh performance electrocatalysts for overall water splitting and oxygen reduction," *Advanced Functional Materials*, vol. 30, no. 47, p. 2000570, 2020.

[36] F. X. Ma, H. B. Wu, B. Y. Xia, C. Y. Xu, and X. W. Lou, "Hierarchical β-Mo2C nanotubes organized by ultrathin nanosheets as a highly efficient electrocatalyst for hydrogen production," *Angewandte Chemie International Edition*, vol. 54, no. 51, pp. 15395–15399, 2015.

[37] M. A. Tekalgne, H. H. Do, T. V. Nguyen et al., "Efficient electrocatalysts for hydrogen evolution reaction using heteroatom-doped MXene nanosheet," *International Journal of Energy Research*, vol. 2023, Article ID 8980888, 11 pages, 2023.

[38] Y. Shi and B. Zhang, "Recent advances in transition metal phosphide nanomaterials: synthesis and applications in hydrogen evolution reaction," *Chemical Society Reviews*, vol. 45, no. 6, pp. 1529–1541, 2016.

[39] B. Weng, C. R. Grice, W. Meng et al., "Metal–organic framework-derived CoWP@C composite nanowire electrocatalyst for efficient water splitting," *ACS Energy Letters*, vol. 3, no. 6, pp. 1434–1442, 2018.

[40] C. Bai, S. Wei, D. Deng, X. Lin, M. Zheng, and Q. Dong, "A nitrogen-doped nano carbon dodecahedron with Co@Co3O4 implants as a bi-functional electrocatalyst for efficient overall water splitting," *Journal of Materials Chemistry A*, vol. 5, no. 20, pp. 9533–9536, 2017.

[41] A. Y. Faid, A. O. Barnett, F. Seland, and S. Sunde, "Ni/NiO nanosheets for alkaline hydrogen evolution reaction: in situ electrochemical-Raman study," *Electrochimica Acta*, vol. 361, no. 2020, article 137040, 2020.

[42] B. Cao, G. M. Veith, J. C. Neuefeind, R. R. Adzic, and P. G. Khalifah, "Mixed close-packed cobalt molybdenum nitrides as non-noble metal electrocatalysts for the hydrogen evolution reaction," *Journal of the American Chemical Society*, vol. 135, no. 51, pp. 19186–19192, 2013.

[43] A. Muthurasu, V. Maruthapandian, and H. Y. Kim, "Metal-organic framework derived Co_3O_4/MoS_2 heterostructure for efficient bifunctional electrocatalysts for oxygen evolution reaction and hydrogen evolution reaction," *Applied Catalysis B: Environmental*, vol. 248, pp. 202–210, 2019.

[44] Y. Zhu, Q. Lin, Y. Zhong, H. A. Tahini, Z. Shao, and H. Wang, "Metal oxide-based materials as an emerging family of hydrogen evolution electrocatalysts," *Energy and Environmental Science*, vol. 13, no. 10, pp. 3361–3392, 2020.

[45] C. M. Kai, C. Kong, F. J. Zhang, D. C. Li, Y. R. Wang, and W. C. Oh, "In situ growth of CdS spherical nanoparticles/Ti_3C_2 MXene nanosheet heterojunction with enhanced photocatalytic hydrogen evolution," *Journal of the Korean Ceramic Society*, vol. 59, no. 3, pp. 302–311, 2022.

[46] V. Kumar, R. K. Mishra, L. G. Trung et al., "Copper, palladium, and reduced graphene oxide Co-doped layered WS_2/WO_3 nanostructures for electrocatalytic hydrogen generation," in *Electronic materials letters*, Springer, 2023.

[47] G. Zhao, K. Rui, S. X. Dou, and W. Sun, "Heterostructures for electrochemical hydrogen evolution reaction: a review," *Advanced Functional Materials*, vol. 28, no. 43, article 1803291, 2018.

[48] B. Darshan, A. Kareem, T. Maiyalagan, and V. Edwin Geo, "$_{CoS2/MoS2}$ decorated with nitrogen doped reduced graphene oxide and multiwalled carbon nanotube 3D hybrid as efficient electrocatalyst for hydrogen evolution reaction," *International Journal of Hydrogen Energy*, vol. 46, no. 27, pp. 13952–13959, 2021.

[49] N.-T. Suen, S.-F. Hung, Q. Quan, N. Zhang, Y.-J. Xu, and H. M. Chen, "Electrocatalysis for the oxygen evolution reaction: recent development and future perspectives," *Chemical Society Reviews*, vol. 46, no. 2, pp. 337–365, 2017.

[50] Y. Xue, S. Sun, Q. Wang, Z. Dong, and Z. Liu, "Transition metal oxide-based oxygen reduction reaction electrocatalysts for energy conversion systems with aqueous electrolytes," *Journal of Materials Chemistry A*, vol. 6, no. 23, pp. 10595–10626, 2018.

[51] R. K. K. Reddy, S. Kailasa, B. G. Rani et al., "Hydrothermal approached 1-D molybdenum oxide nanostructures for high-performance supercapacitor application," *SN Applied Sciences*, vol. 1, no. 11, pp. 1–9, 2019.

[52] F. Soofivand, M. Sabet, H. Seyghalkar, and M. Salavati-Niasari, "Using the $[Co(oct)_2]$ as a new precursor for simple synthesis of CoS_2 nanoparticles and kinetics studies on photocatalytic activities under UV irradiation," *Journal of Nanostructures*, vol. 8, pp. 75–81, 2018.

[53] C. Liang, X. Zhang, P. Feng, H. Chai, and Y. Huang, "ZIF-67 derived hollow cobalt sulfide as superior adsorbent for effective adsorption removal of ciprofloxacin antibiotics," *Journal of Chemical Engineering*, vol. 344, pp. 95–104, 2018.

[54] X. Zheng, J. Xu, K. Yan, H. Wang, Z. Wang, and S. Yang, "Space-confined growth of MoS2 nanosheets within graphite: the layered hybrid of MoS2 and graphene as an active catalyst for hydrogen evolution reaction," *Chemistry of Materials*, vol. 26, no. 7, pp. 2344–2353, 2014.

[55] H. Khan, S. A. Shah, W. U. Rehman, and F. Chen, "CoS2Nanoparticles-Decorated MoS_2/rGO nanosheets as an efficient electrocatalyst for ultrafast hydrogen evolution," *Advanced Mateials Interfaces*, vol. 9, no. 1, article 2101294, 2022.

[56] J. Chu, G. Sun, X. Han et al., "Ultrafine CoO nanoparticles as an efficient cocatalyst for enhanced photocatalytic hydrogen evolution," *Nanoscale*, vol. 11, no. 33, pp. 15633–15640, 2019.

[57] L. Pang, A. Barras, Y. Zhang et al., "CoO promoted the catalytic activity of nitrogen-doped MoS2 supported on carbon fibers for overall water splitting," *ACS Applied Materials Interfaces*, vol. 11, no. 35, pp. 31889–31898, 2019.

[58] P. Cheng, C. Yuan, Q. Zhou et al., "Core–shell MoS_2@CoO electrocatalyst for water splitting in neural and alkaline solutions," *The Journal of Physical Chemistry C*, vol. 123, no. 10, pp. 5833–5839, 2019.

[59] D. Kong, H. Wang, Z. Lu, and Y. Cui, "CoSe2 nanoparticles grown on carbon fiber paper: an efficient and stable electrocatalyst for hydrogen evolution reaction," *Journal of the American Chemical Society*, vol. 136, no. 13, pp. 4897–4900, 2014.

[60] Z. Chen, D. Cummins, B. N. Reinecke, E. Clark, M. K. Sunkara, and T. Jaramillo, "Core–shell MoO_3–MoS_2 nanowires for hydrogen evolution: a functional design for electrocatalytic materials," *Nano Letters*, vol. 11, no. 10, pp. 4168–4175, 2011.